RaLiBEV: Radar and LiDAR BEV Fusion Learning for Anchor Box Free Object Detection Systems

Yanlong Yang*, Jianan Liu*†, Tao Huang, Senior Member, IEEE, Qing-Long Han, Fellow, IEEE, Gang Ma, and Bing Zhu, Member, IEEE

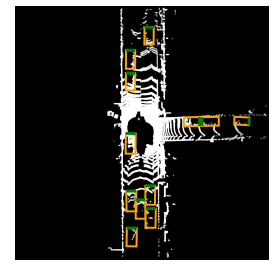
Abstract—In autonomous driving systems, LiDAR and radar play important roles in the perception of the surrounding environment. LiDAR provides accurate 3D spatial sensing information but cannot work in adverse weather like fog. On the other hand, the radar signal can be diffracted when encountering raindrops or mist particles thanks to its wavelength, but it suffers from large noise. Recent state-of-the-art works reveal that fusion of radar and LiDAR can lead to robust detection in adverse weather. The existing works adopt convolutional neural network architecture to extract features from each sensor data stream, then align and aggregate the two branch features to predict object detection results. However, these methods have low accuracy of bounding box estimations due to a simple design of label assignment and fusion strategies. In this paper, we propose a bird's-eye view fusion learning-based anchor boxfree object detection system, which fuses the feature derived from the radar range-azimuth heatmap and the LiDAR point cloud to estimate the possible objects. Different label assignment strategies have been designed to facilitate the consistency between the classification of foreground or background anchor points and the corresponding bounding box regressions. In addition, the performance of the proposed object detector is further enhanced by employing a novel interactive transformer module. The superior performance of the proposed methods in this paper has been demonstrated using the recently published Oxford radar robotCar dataset, showing that the average precision of our system significantly outperforms the best state-of-the-art method by 14.4% and 20.5% at IoU equals 0.8 in clear and foggy weather testing, respectively.

Index Terms—ADAS, autonomous driving, anchor box free object detection, LiDAR, point cloud, radar, range-azimuth heatmap, label assignment, BEV fusion, interactive transformer, deep learning

I. INTRODUCTION

UTONOMOUS driving systems generally utilize sensors such as LiDAR, camera, and radar to build the perception functionality. Such perception scheme is wildly demonstrated by massive amounts of works in several aspects, such as data collection/generation [1][2], algorithm development [3][4] and real-world testing [5]. LiDAR provides rich semantic and geometry information for environmental perception tasks

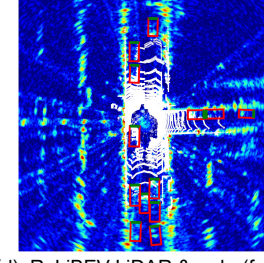
- *Both authors contribute equally to the work and are co-first authors. †Corresponding author.
- Y. Yang and G. Ma are with Vanjee Technology, Beijing, P.R. China.
- J. Liu is with Vitalent Consulting, Gothenburg, Sweden. Email: jianan.liu@vitalent.se.
- T. Huang is with the College of Science and Engineering, James Cook University, Smithfield QLD 4878, Australia. Email: tao.huang1@jcu.edu.au.
- Q.-L. Han is with the School of Science, Computing and Engineering Technologies, Swinburne University of Technology, Melbourne, VIC 3122, Australia. Email: qhan@swin.edu.au.
- B. Zhu is with the School of Automation Science and Electrical Engineering, Beihang University, Beijing 100191, P.R. China. Email: zhubing@buaa.edu.cn.





(a). Ground-truth LiDAR only(clear)

(b). Ground-truth LiDAR only(foggy)



(c). Ground-truth LiDAR & radar(foggy) (d). RaLiBEV LiDAR & radar(foggy)

Fig. 1. Performance of our RaLiBEV in clear and foggy weather. The LiDAR and radar visualization results are combined by radar range azimuth heatmap with jet pseudo-color in the background and LiDAR with white point cloud and 2D object bounding boxes. The ground truth boxes are orange, and the predicted boxes by RaLiBEV are red. All the boxes use green lines to indicate the heading direction.

[6][7], including object detection [8][9], multi-object tracking [10][11], ego localization [3][12] and mapping [13]. To build a robust perception system for autonomous driving, recent works show that the fuse of LiDAR and camera at the raw data stream level can significantly improve the perception capability [14][15]. However, the performance of either camera or LiDAR can severely drop in adverse weather, i.e., rain, snow, and fog [16][4]. For example, the camera can be blurred, LiDAR's operating range might be greatly shortened, and the number of noise points might be greatly increased due to the impact of heavy snow or fog. As shown in Fig. 1(b), the noisy points around the ego vehicle arise while the far end LiDAR points disappear, compared to the LiDAR point cloud measured in the clear weather, as shown in Fig. 1(a).

In contrast with cameras and LiDAR, radar can naturally avoid the influence of adverse weather since the millimeter wavelength signals can be diffracted in the rain, snow, and fog. Such characteristic makes radar a powerful complementary sensor in addition to either camera or LiDAR. The typical Frequency Modulated Continuous Wave (FMCW) radar, widely used in automotive systems, can accurately separate objects in range and speed dimension but has a low angular resolution due to the limited number of antennas in the compact space.

Thus, radar can only provide many sparser detection points with ambiguity in angular information compared to the dense LiDAR point cloud. Such a drawback caused limitations on its performance when applied in the perception system. To take full advantage of the robustness of radar in adverse weather, radar range-azimuth heatmap rather than detection points has been employed to fuse with LiDAR point cloud for vehicle detection in the recent proposed anchor boxbased methods [17][18]. However, their methods suffer from generalization issues since their approaches require predefined anchor boxes and they need to be carefully chosen according to the dataset. Moreover, these methods have been shown to have unsatisfactory performance, especially in the performance with high accuracy requirements. To address these issues, we propose RaLiBEV, a Radar and LiDAR BEV Fusion-based anchor box-free object detector.

In RaLiBEV, the LiDAR point cloud is pillarized [8] to build a structured data format in BEV, while the radar range-azimuth heatmap is naturally discrete sampling under BEV. Then the BEV feature maps from radar and LiDAR are extracted separately and fused together to form the aggregated BEV feature map. This aggregated BEV feature map is then forwarded to the backbone of the network. Finally, the feature map delivers into an anchor box-free multi-scale detection head to decode the estimated bounding boxes of vehicles. On the one hand, different from the anchor box-based scheme, the anchor box free detection head is designed to find the represented pixels, i.e., key points among all the anchor points, in the predicted feature map first. Then, these pixels are used as a positive sample to regress the remaining feature channels. This scheme brings the inconsistency of the foreground/background classification, and regression problem [19] that the key point with a high classification score does not always lead to better accuracy in the regression of the bounding box. On the other hand, how to fuse the extracted feature information from fruitful radar range-azimuth heatmap with LiDAR feature map in a more effective and complementary manner, rather than concatenate them together, is also an open question. To solve the aforementioned issues, novel label assignment strategies have been proposed upon the RaLiBEV framework to mitigate the inconsistency of the foreground and background classification and regression. Meanwhile, interactive transformerbased BEV fusion approaches are designed to explore better the interaction between radar and LiDAR feature maps for RaLiBEV.

The main contributions of this paper are concluded as below:

- A radar and LiDAR BEV fusion-based anchor box free object detector, RaLiBEV, is proposed. The RaliBEV can generate accurate 2D bounding boxes in BEV by fusion of features extracted from the radar range-azimuth heatmap and the LiDAR point cloud.
- A novel label assignment strategy, Gaussian Area-based Consistent Heatmap and intersection over union (IoU) Cost Positive Sample Assignment (GACHIPS), is proposed to combat the inconsistency between the classification of key points and the corresponding bounding box regression tasks in the anchor box free object detector.

- A novel interactive transformer-based fusion module, Dense Query Map-based Interactive BEV fusion (DQMITBF), is proposed to fuse radar and LiDAR feature maps. With the introduction of dense learnable queries, the fusion module provides more flexibility to query the suitable features from both maps to fuse.
- The aforementioned object detector can achieve fairly accurate detection performance even in adverse weather, as shown in of Fig. 1(d) compared to the ground truth bounding boxes illustrated in Fig. 1(c) which outperforms the state-of-the-art radar and LiDAR fusion-based object detector with a large margin in the popular Oxford Radar RobotCar (ORR) dataset [1].

The rest of this paper is organized as follows. Section II discusses the related works, including LiDAR-based perception methods, radar-based perception methods, and the methods which fuse radar and LiDAR for object detection. In Section III, the proposed radar and LiDAR fusion-based object detection approach, RaLiBEV, is introduced. In addition, the proposed label assignment strategies and interactive transformer-based fusion schemes are also described. Then, the experiment process and corresponding results on ORR datasets are explained and analyzed in Section IV. Finally, the conclusion and further work are drawn in Section V.

II. RELATED WORKS

A. LiDAR-based Object Detection

LiDAR is a widely used sensor in surrounding environment perception, and object detection is one of the most important missions in environment perception. The LiDAR object detection method based on deep learning can be divided into four categories according to the processing approach on the input point cloud.

The first approach is the point-based method. It implements a linear layer to extract features on unordered point cloud [20][21]. The second approach is the grid-based method. This method discretizes the point cloud into 2D grids or 3D voxels, then applies CNN for further feature extraction [22][8]. The third approach is the graph-based method, which transforms point cloud as graph data format [23]. The Graph Neural Network (GNN) is employed for extracting the feature and detecting the objects, where the points are defined as vertices and the relations between points are defined as edges. The fourth type is the combination method. One way is to combine features extracted from two different representations of the point cloud, such as points features and grid/voxel features [24]. Another way is to concatenate features from different views of 2D grids, such as range view and BEV, and decode concatenated features by 2D CNN afterward.

Although LiDAR can provide precise and dense 3D spatial information, the inherent problem of facing adverse weather still limits its performance.

B. Radar-based Object Detection

Radar can overcome the negative effect caused by adverse weather because it uses under-millimeter wave band electromagnetic signals. The approaches addressing radar object detection under noise can be generally classified as conventional and deep learning methods.

The conventional method applies an adaptive peak extraction algorithm to pick the possible object points as detection from radar signals [25], then the clustering [26] is utilized to suppress the noise further and estimate the objects. This method provides fast radar object detection results. However, the conventional method has limited performance and lacks object geometry information.

Modern deep-learning methods can be applied to either radar detection points or signals. When dealing with radar detection points, usually linear layers are used to extract points feature [27][28][29]. When dealing with radar signals, the conventional adaptive peak extraction and clustering algorithm are processed via deep learning. Besides, since the raw radar signal forms a structured format, the CNN block can be conveniently applied. [30][31] propose a two-stage method of first cropping the range-azimuth heatmap area, second classifying the objects by CNN.

However, due to the inside of the circuit and various electromagnetic radiation from the environment, the performance of radar-only-based object detection cannot meet the requirements of autonomous driving.

C. Radar and LiDAR Fusion-based Object Detection

Radar and LiDAR both have their strength and weaknesses. Fusing the information from the two types of sensors can achieve a better surrounding perception [17][18]. Generally, sensor fusion can be performed at the result or feature levels.

In result-level fusion, each sensor is characterized as an individual detection union. Then the detected objects are collected to generate the final result. This method consumes less transmission bandwidth and has a fast operation speed. However, its performance is severely limited by each single sensor detector.

In feature-level fusion, the deep learning-based method is often applied. The deep learning neural network extracts the features from the two sensor data. Then the extracted features are aligned and fused.

To solve sensor perception in adverse weather, the Deep Entropy Fusion (DEF) [32] is the pioneering work that fuses LiDAR, radar, and camera together and shows marginal performance under a foggy scenario. However, the radar data in this work has a low-angle resolution, which can not provide a satisfactory sensing supplement. Another work, MVDNet [17], fuses the high angular resolution radar raw signal data with LiDAR point cloud. In the fusion step, MVDNet applies a transformer module to fuse feature vectors from two branches as spatial cross-fusion. Then it fuses features from continuous frames as temporal fusion for further improvement. However, the performance of this work is limited due to the simple label assignment strategy in the loss computation procedure, as well as the region-of-interest (ROI) assisted fusion design. The successive work, ST-MVDNet [18], improves the performance of MVDNet. However, this work considers more about the sensor failure problem. It leverages mutual learning and

designs two identical models: the teacher and student models. The teacher model takes two valid data streams of radar and LiDAR and generates predicted results to supervise the student model. While the student model takes randomly missing LiDAR or radar data as input. The student model passes model parameters to the teacher model in each training iteration using an exponential moving average (EMA). This work illustrates the possibility of addressing sensor failure problems. Still, it ignores the performance degradation of MVDNet caused by simple label assignment and fusion design, especially in terms of high-precision detection results.

III. PROPOSED METHOD

In this section, the framework of the proposed anchor box-free radar and LiDAR fusion-based object detector are first introduced. Then, two enhancements of RaLiBEV, one with label-assignment strategies and the other with interactive transformer fusion strategies, are described.

A. Anchor Box Free Object Detection

Following the idea of sensor fusion, aggregating features from each sensor under BEV representation is straightforward. Therefore, based on the YOLOv4 [33] backbone, an anchor box-free radar and LiDAR BEV object detector (RaLiBEV) is proposed, as shown in Fig. 2. The corresponding LiDAR point cloud and radar range-azimuth heatmap are used as input data. Then the aggregated features are forwarded into the YOLOV4 backbone for further processing. Finally, a multi-scale anchor box free detection head is employed to decode the 2D BEV rotating bounding boxes detection result.

For the radar data, the strength of the range-azimuth heatmap represents the possibility of object existence under the BEV space. Where the object exists, the energy of the heatmap would be greater than that of the empty area. The radar data is converted from polar to Cartesian coordinates by applying bilinear interpolation, so the final structure shape of the data shows as $[W_r, H_r, C_r]$. For LiDAR data, since the point cloud is an unordered 3D point set, the data needs to be structured before subsequent operations. Therefore the method of PointPillar [8] is applied to form the input LiDAR data into a fixed shape $[W_l, H_l, C_l]$ under BEV.

After the pre-processing, N convolution layers on each branch are applied to extract features without downsampling. Then two branch data are fused with an interactive transformer and sent into the YOLOv4 backbone for further feature extraction.

A multi-scale anchor-free detection head is added at the end to decode the detection result. The first output channel of the detection head is a predicted heatmap, representing the object's existence probability. The second to the last channel represents $\triangle x$, $\triangle y$, width, length, angle class, angle offset, and object class, respectively. $\triangle x$ and $\triangle y$ represents the predicted box center offset in x and y direction. Two channels are set to help angle regression. One is an angle classification channel, the other is an angle offset regression channel.

Following the state-of-the-art anchor-free detection paradigm, the anchor points of the feature map should be

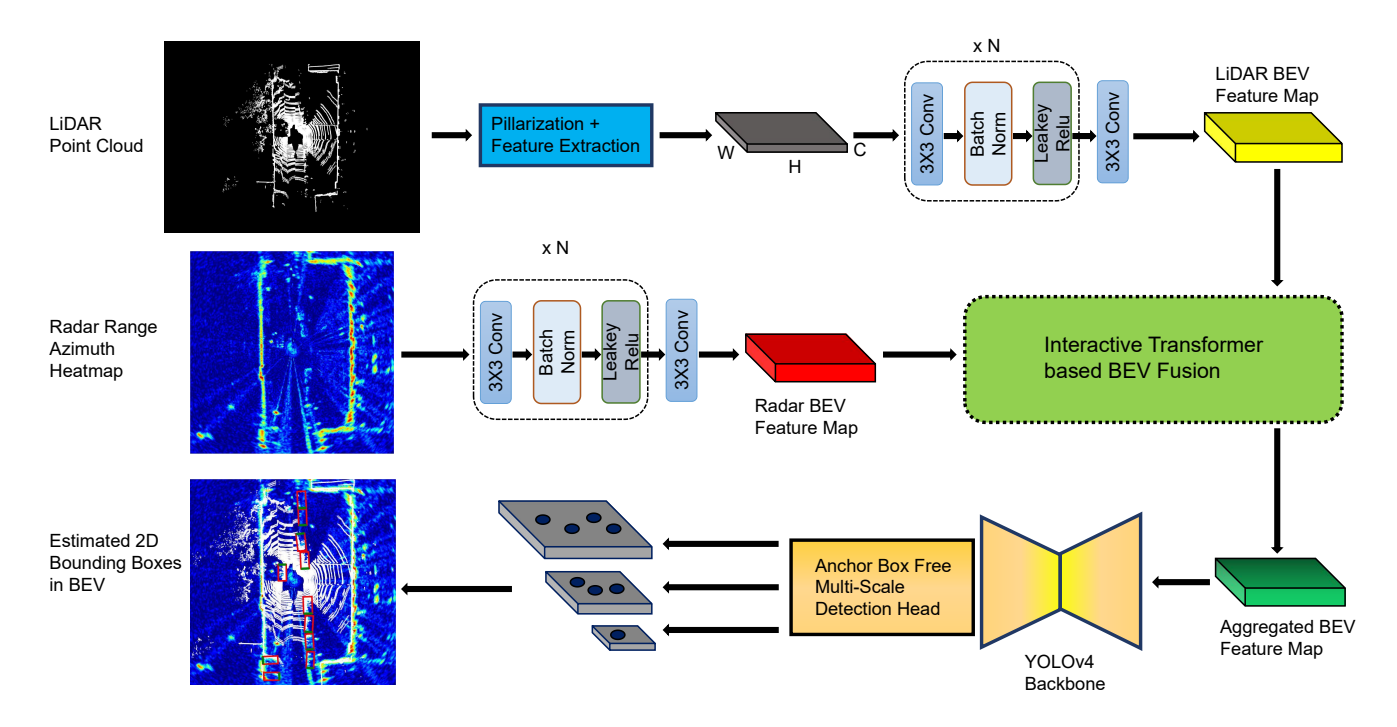


Fig. 2. The entire pipeline of proposed radar and LiDAR fusion-based anchor box free object detector, RaLiBEV.

specified first, then start regression based on those locations. The 2D ground truth label boxes generate a Gaussian distribution map as a supervision signal under each output head scale to train the network for heatmap estimation in a supervised manner. This method can be described by:

$$G(X|\mu,\Sigma) = \frac{1}{2\pi^{\frac{d}{2}}|\Sigma|^{\frac{1}{2}}} e^{-\frac{1}{2}(X-\mu)^T \Sigma^{-1}(X-\mu)}$$
(1)

where the X is the 2D BEV spatial vector, d is the dimension of X. μ is the mean of X, which is the center coordinates of ground truth boxes. Σ is a covariance matrix of the distribution, which can be calculated by:

$$\Sigma = E(X - E(X))(X - E(X))^{T}$$
(2)

where the four corners' 2D coordinates of a box are used as x, and the E(x) equals the center coordinates of the box. Iteration is done over all the ground truth objects in one frame to generate the ground truth Gaussian heatmap.

B. Label Assignment Strategies

For an object detection problem, the loss, in general, can be described as the sum of classification loss and regression loss, as shown here:

$$\mathcal{L} = \mathcal{L}_{cls} + \alpha \mathcal{L}_{reg} \tag{3}$$

where the \mathcal{L}_{cls} is the classification loss implemented with focal loss [34], the \mathcal{L}_{reg} is the regression loss implemented with smooth L1 loss, α is the weight of regression loss. The focal loss is modified with Gaussian distribution weight \mathbf{G}_{ij} ,

and the weight of regression loss α is a sectional function, respectively:

$$\mathcal{L}_{cls} = \begin{cases} -\sum_{i,j=0}^{N} \mathbf{G}_{i,j} (1 - p_{i,j})^{\gamma} log(p_{i,j}) & \text{if } \mathbf{G}_{i,j} = 1, \\ -\sum_{i,j=0}^{N} \mathbf{G}_{i,j} p_{i,j}^{\gamma} log(1 - p_{i,j}) & \text{otherwise,} \end{cases}$$
(4)

$$\alpha_{ij} = \begin{cases} 1 & \text{if } \mathbf{G}_{i,j} = 1, \\ 0 & \text{otherwise,} \end{cases}$$
 (5)

where $G_{ij} \in [0,1]$ specifies the supervision Gaussian distribution heatmap generated from (1), and $p_{ij} \in [0,1]$ is the model's estimated heatmap value for each anchor point in a feature map. γ is a static parameter that balances the weight of positive and negative samples. $\alpha_{i,j} \in \{0,1\}$ indicates only the anchor point $p_{i,j}$ locates at $G_{i,j} = 1$ position which is identified as positive sample shall contribute to the final loss.

The above discussion shows that the regression loss could only occur on the positive samples, while the classification loss is computed upon every anchor point on the feature map. This leads to the problem that when decoding the predicted object, an anchor point with a higher classification score does not always index the best bounding box regression result. This is known as the inconsistency problem in label assignments. A label assignment strategy with lesser inconsistency between classification and regression can decrease the model's missdetection rate and help achieve higher detection accuracy.

Typically, three strategies of label assignment could be applied, including bipartite matching, multi-positive label assignment, and single-positive label assignment. The 'multi/single' indicates how many anchor points can be chosen as the positive sample for one object.

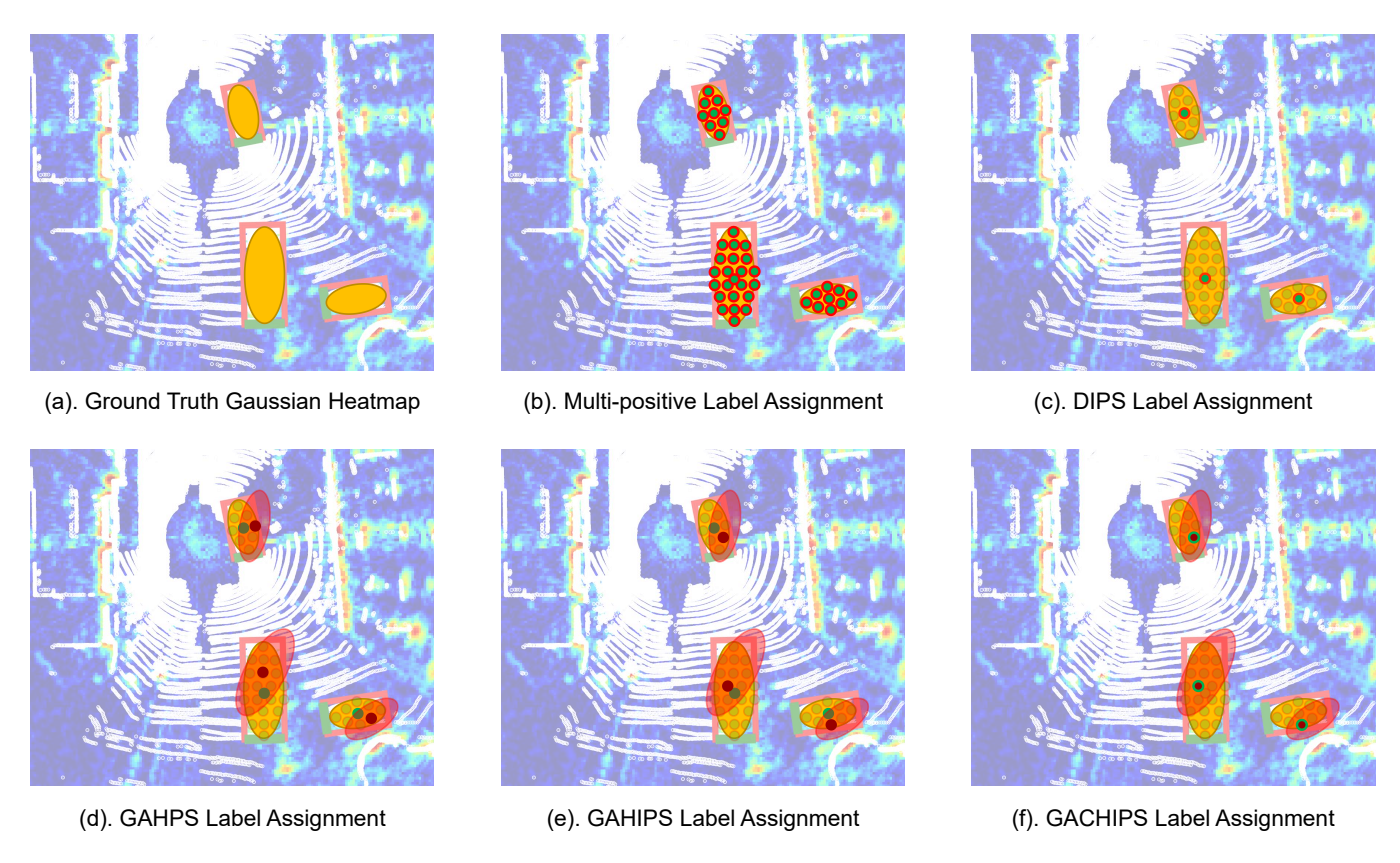


Fig. 3. Label assignment strategies. The ground truth heatmap defines the orange-colored region of target objects. The red ellipses are prediction heatmap Gaussian distribution. The green and red dots represent the classification and regression key points.

- 1) Bipartite Matching Label Assignment: The typical bipartite matching label assignment is based on the Hungarian algorithm. This set-based label assignment builds a cost matrix of IoU between predicted and ground truth boxes, where the predicted boxes are decoded from a predefined location. Then it finds the best matching positive samples by the Hungarian algorithm. The traditional bipartite matching process is based on anchors [35], while DETR [36] leveraging object query changes this matching art to a total end-to-end style. Using the Hungarian algorithm, DETR computes loss directly between predefined object queries and ground truth object boxes. Then after training, the converged queries can be directly decoded into the final predicted box without Non-Maximum Suppression (NMS). However, the size of the query map in the proposed method is set to be the same as the size of the radar and LiDAR feature map. Such a large number of queries leads to massive computational consumption, which is not feasible when applying the Hungarian algorithm. Thus, such bipartite matching label assignment is not considered for our proposed method.
- 2) Multi-Positives Label Assignment: Following the idea that multiple positive anchor points may alleviate positive and negative sample imbalance problems in anchor-free detection architecture, a Gaussian area-based multi-positive label assignment is designed. Based on the ground truth Gaussian heatmap G created in section III-A, a static threshold is used to extract the specific region as the positive anchor points. Classification and regression are then applied together on each

positive anchors points. As Fig. 3(b) shows, all these dots with green and red colors overlapped are the selected positive samples. The classification and regression both happened on the same key points. They are all located in the ground truth Gaussian distribution orange-colored area.

However, more positive samples may exacerbate the inconsistency between the foreground and background classification and regression, as the multi-positive strategy can help with object existence classification but introduces a larger gap between classification and regression. The experiment result is shown later in Section IV-C1

- 3) Single Positive Label Assignment: Due to the enlarged inconsistency problem introduced by multi-positive label assignment, the single-positive label assignment strategy is considered. Inspired by CenterPoint [9], four types of single positive label assignment strategies are designed below.
 - The first design is *direct index based positive sample* (DIPS) assignment, which is our baseline method. DIPS treats the label center locations as the positive anchor points, then applies classification and regression on these anchor points. As Fig. 3(c) shows, only the center anchor point in each ground truth Gaussian distribution area is chosen as a positive sample. Then the classification and regression are all based on the same key points.
 - The second design is Gaussian area-based heatmap cost positive sample (GAHPS) assignment. As illustrated in Fig. 3(d), the classification and regression are based on different key anchor points. First, the prediction heatmap

is influenced by the model to compute the classification loss with the ground truth Gaussian heatmap. The green dots in orange color ellipses illustrate the classification key anchor points. After the heatmap loss is computed, the peak value anchor points of the prediction heatmap in red color are chosen as the regression positive anchor points. This strategy ensures that only the best classification position contributes to the loss result of regression throughout the training process.

- The third design is Gaussian area-based heatmap and IoU cost positive sample (GAHIPS) assignment. This method is a divergence from the previous one. As shown in Fig. 3(e), the same as GAHPS, GAHIPS applies the classification loss firstly at the green key anchor point. Then GAHIPS inferences the prediction heatmap the same as GAHPS. Unlike GAHPS, GAHIPS regression positive sample point is no longer only the peak position of the predicted heatmap but also the location where the peak plus the predicted best IoU box exists. Therefore, this strategy attempts to let regression participate in label assignment so that classification and regression simultaneously act on loss to guide model training.
- The fourth design is Gaussian area-based consistent heatmap and IoU cost positive sample (GACHIPS) assignment, which is a divergence of the third strategy. Previous strategies have a feature that the classification positive sample position is designed to converge to the center of the ground truth box. The regression positive sample position moves with the former. These strategies build a weak relation between classification and regression. However, it does not mean that the positive sample position must be the center of the ground truth box. Therefore, inheriting the idea of GAHIPS, the classification positive sample position is moved to the regression positive sample position as illustrated in Fig. 3(f). The training includes two steps. First, inference forwardly to decode boxes of all the candidate anchor points in each ground truth Gaussian distribution area. Second, pick the points with the maximum heatmap value plus IoU (prediction box with ground truth boxes) as the positive sample, then apply classification and regression loss.

Based on the above assigning result, the loss function is specified below. The heatmap loss is calculated by focal loss. For feature channels such as $\triangle x$, $\triangle y$, width, length, and angle offset, we use smooth L1 loss. While for feature channels such as the angle class, the cross-entropy loss is applied. Then all the losses are sum together with weights α as:

$$L = l_h^{fl} + \alpha (l_{\triangle xy}^{reg} + l_{wl}^{reg} + l_{\theta}^{ce} + l_{\triangle \theta}^{reg}). \tag{6} \label{eq:6}$$

When making an inference, the first thing to do is to extract peaks from the predicted heatmap. We set a static threshold to pick every anchor point to generate the corresponding box. Then utilize NMS to discard other boxes that overlap with the higher-confidence box by a certain size. Beware that NMS can still filter out a certain amount of overlapping bounding boxes estimated from three branches in multiple scales. However, the estimated bounding boxes rarely overlap in a single scale

branch since the anchor box-free approach with a single-positive label assignment strategy is employed.

C. Interactive Transformer for Fusion of Radar and LiDAR in BEV

The simplest way to fuse two sensors' data is by concatenating features from each sensor. However, this method has limited performance because it can not weigh the feature well. To fuse two branch data more reasonably, we design an interactive transformer-based BEV Fusion block [37]. As shown in Fig. 4, two different fusion logic are presented. Fig. 4(a) describes a direct interactive BEV fusion, which utilizes one sensor branch feature map as query, and the other one as key and value. The weight matrix is calculated by matrix multiplication of the query and key, then fed into a softmax for normalization. This operation is the interactive attention process. Finally, generate the dot product of the weight and value, where the value is concatenated feature map. The above procedure can be described below:

$$\boldsymbol{X}_{out} = \sigma(\boldsymbol{X}_{s_0} \boldsymbol{X}_{s_1}^T) \odot \boldsymbol{X}_{s_1} + \boldsymbol{X}_{s_1}$$
 (7)

where X is the feature map, $\sigma(\cdot)$ is the softmax function, s_0 , s_1 belongs to different sensors playing the role of query and key.

The second one in Fig. 4(b) shares a similar idea with Fig. 4(a) while owning a different part in the query definition. Here we define a random initialized learnable query, which shares the same size as the input key feature map. Here the interactive attention is calculated between learnable query and concatenated radar and LiDAR feature map, which is regarded as the key. The mathematical expression can be described as:

$$\boldsymbol{X}_{out} = \sigma(\boldsymbol{X}_{C} \boldsymbol{X}_{C}^{T}) \odot \boldsymbol{X}_{C} + \boldsymbol{X}_{C}$$
 (8)

where X_Q is the random initialized learnable query, and X_C is concatenated feature map of radar and LiDAR.

IV. IMPLEMENTATION AND RESULTS

A. Dataset and Evaluation Metrics

The ORR dataset [1] is selected because it provides a synchronized LiDAR point cloud, radar range azimuth heatmap, car motion pose parameters, etc. The LiDAR point cloud was captured by two Velodyne HDL-32E LiDARs, each designed to cover one side of the car. On the top of the car locates a NavTech CTS350-X radar, which has a 360° field of view in the fashion of a mechanical scan. The angle resolution of radar data is 0.9° every 400ms, while LiDAR data angle resolution is 0.33° every 20ms.

The synchronization issue between LiDAR data and radar data and the annotation generation was solved by interpolation with the help of ego car pose parameters [17]. Specifically, the pose parameters compensated for the misalignment between the LiDAR point cloud and radar range-azimuth heatmap. Utilizing the timestamps as a reference, [17] computes the motion between LiDAR point cloud and radar heatmap, then transfer every point to radar coordinate. The annotation bounding boxes are also created by [17] every 20 frames. The remaining

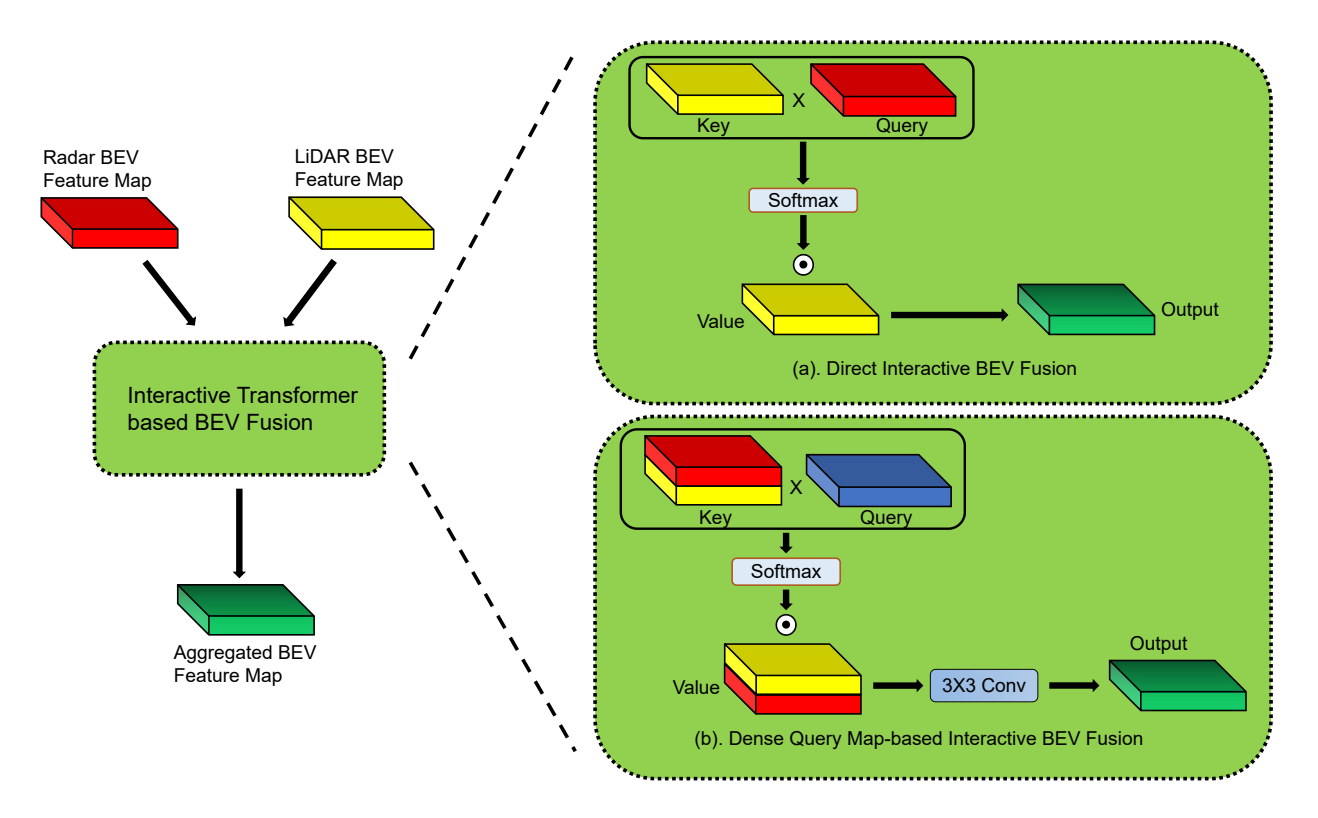


Fig. 4. Interactive transformer BEV fusion approaches.

frames' annotations were also generated by interpolation. For testing in a foggy scenario, MVDNet relocates the LiDAR point cloud with the method of DEF [32]. According to the fog model in DEF, MVDNet sets the fog probability to 0.5 to recompute a maximum visible range for every point. If the current point range is greater than the maximum foggy range, this point would be set rather lost or relocated as a scatter point. Following the same operations on data in MVDNet, the 2D label bounding boxes are used as supervision. Corresponding radar and LiDAR data in 8862 number frames are split into 7071 for training and 1791 for testing.

To evaluate the prediction result of the model, the 2D rotated bounding box average precision (AP) under different IoU thresholds is employed as a final evaluation metric. This metric simultaneously evaluates the precision and recall performance of the model under the test dataset. A higher AP value represents better prediction precision of the bounding box and a smaller missing detection rate of the objects. Prediction boxes can be defined as True Positive (TP) objects, which overlap with the ground truth objects over the IoU threshold, or False Positive (FP) objects which overlap with ground truth objects lesser than the IoU threshold. By setting different IoU thresholds, the number of TP and FP objects varies. Under a certain IoU threshold value, all the prediction boxes can be arranged as a TP/FP list sorted by their class scores. The precision and recall performance is defined as (9):

$$Precision = \frac{TP}{TP + FP}$$

$$Recall = \frac{TP}{TP + FN}$$
(9)

TABLE I EXAMPLE LIST OF PR CURVE AT IOU=0.5

Scores	0.98	0.97	0.96	0.95	0.94	0.92	0.91
Prediction Objects	TP	TP	FP	TP	TP	TP	FP
Precision	1	1	2/3	3/4	4/5	5/6	5/7
Recall	1/5	2/5	2/5	3/5	4/5	1	1

where the TP+FP equals the total number of prediction objects, and the FP is the number of false prediction objects. While the FN is the number of miss-detection objects, TP+FN equals the number of ground truth objects.

The table I shows an example of how the AP is calculated by setting the IoU threshold as 0.5. Assuming no miss-detected objects exist, all these predicted objects represented in the column are sorted by their scores. Precision and recall are computed according to (9) in each column. It is worth mentioning that the precision result drops and the recall increase, along with the decrease of the object's scores. The AP@IoU=0.5 is then defined as the area value enclosed under the precision-recall curve accordingly to reflect the trend of the precision-recall curve as a performance metric. The greater the AP value is, the better model performs.

B. Implementing Details

The preprocess of LiDAR data is based on point pillar [8], where we set $0.2m \times 0.2m$ as our BEV spatial resolution. It transforms the disordered LiDAR point cloud to a $320 \times 320 \times 9$ structured matrix. Meanwhile, the input radar data is in the format of $320 \times 320 \times 1$ under BEV, naturally. As Fig. 2

TABLE II
ABLATION STUDY OF RALIBEV ANCHOR BOX FREE OBJECT DETECTOR.

Methods	AP@IOU=0.5	AP@IOU=0.65	AP@IOU=0.8						
Proposed RaLiBEV with Different Label Assignments and Plain BEV Fusion (Ours)									
Gaussian Area-based Multi-Positives Sample Assignment	95.4	94.2	75.7						
Direct Index-based Positive Sample Assignment (DIPS)	96.3	94.9	84.5						
Gaussian Area-based Heatmap Cost Positive Sample Assignment	96.7	95.4	89.5						
Gaussian Area-based Heatmap and IoU Cost Positive Sample Assignment	96.8	96.7	92.0						
Gaussian Area-based Consistent Heatmap and IoU Cost Positive Sample Assignment (GACHIPS)	97.4	96.7	93.9						
Proposed RaLiBEV with Interactive Transformer-based BEV Fusion (Ours)									
Direct Interactive Transformer for BEV Fusion	97.8	97.5	92.3						
Dense Query Map-based Interactive Transformer for BEV Fusion (DQMITBF)	98.8	97.7	94.8						

TABLE III

COMPARISON OF AP OF ORIENTED BOUNDING BOXES IN BIRD'S EYE VIEW BETWEEN OUR PROPOSED RALIBEV AND STATE-OF-THE-ART METHODS.

THE NUMBERS IN BOLD ARE THE BEST OF ALL METHODS.

	Train	Clear+Foggy					Clear-only						
Method	Test	Clear		Foggy			Clear			Foggy			
	IoU	0.5	0.65	0.8	0.5	0.65	0.8	0.5	0.65	0.8	0.5	0.65	0.8
PointP	PointPillar (CVPR 2019) [8] 85.8 83.0 58.3		72.8	70.3	48.6	85.8	82.9	60.6	71.3	68.3	47.8		
DEF	(CVPR 2020) [32]	86.6	78.2	46.2	81.4	72.5	41.1	85.9	78.1	44.2	71.8	63.7	32.4
MVDN	Vet (CVPR 2021) [17]	90.9	88.8	74.6	87.4	84.6	68.9	87.2	86.1	72.6	78.0	75.9	61.6
ST-MVE	ONet (CVPR 2022) [18]	94.7	93.5	80.7	91.8	88.3	73.6	91.4	89.9	78.4	81.2	80.8	64.9
RaLiBEV	with GACHIPS (Ours)	97.8	97.7	93.9	97.8	96.7	93.7	97.4	96.7	93.9	84.6	82.4	73.8
RaLiBEV	with DQMITBF (Ours)	98.8	97.7	95.1	97.9	97.8	94.1	98.8	97.7	94.8	83.3	80.9	70.6

shows, the subsequent convolution block consists of a 3×3 convolution layer, a batch norm layer, and a leaky ReLu layer. The replication N of it is set as 3. The inference procedure decodes the predicted boxes from three scale output anchorfree heads. The static threshold is set to 0.1 to extract peaks (as key points among all anchor points) from the predicted heatmap. After generating boxes from three scale output feature maps, the NMS method is applied for deleting extra boxes, whose threshold is set as 0.2.

When training, the batch size is set to 32, and 4 Nvidia Tesla V100S GPUs are used. The first two epochs are used as a warming up. The learning rate linearly increases from 0 to 0.01 after 2 epochs' iterations and then decreases by a ratio of 0.1 every 10 epochs. ADAM optimizer is used in the training process.

C. Experimental Results and Analysis

1) Ablation Study on Label Assignment Strategies: Experiments on Oxford Radar RobotCar dataset are performed to evaluate the effectiveness of the proposed strategies. The evaluation metrics of AP at IoU 0.5, 0.65, and 0.8 are chosen to demonstrate changes in performance.

Table II presents the experiment results of different label assignment strategies and interactive transformer fusion architectures of our proposed RaLiBEV. It should be noted that since the annotation has only one type of labeled car class, the AP is used only for cars. The performance of the **Gaussian Area-based Multi-Positive Sample Assignment** strategy based on the RaLiBEV shows a basic improvement. The AP of IoU of 0.5 and 0.65 is 95.4% and 94.2%, both

improve approximately 4%, but show a 2.7% drop of AP at IoU of 0.8, falling down to 75.7% compared to the ST-MVDNet. The AP performance of the state-of-the-art ST-MVDNet at IoU 0.5, 0.65, and 0.8 are 91.4%, 89.9%, and 78.4%, respectively.

The second type of label assignment strategy is **Direct** Index-based Positive Sample (DIPS) Assignment. This strategy presents improvement not much at the low precision AP result at IoU of 0.5 and 0.65, about 0.7% - 0.9%. Still, better performance at high precision AP at IoU of 0.8 results about 6% compares to the first strategy above. The result of the third strategy illustrates the effectiveness of choosing a more appropriate positive-sample strategy. Compared to the previous strategy, the performance of Gaussian Area-based Heatmap Cost Positive Sample (DAHPS) Assignment shows another performance improvement of about 5% in high precision, which reaches 89.5% AP at IoU of 0.8. Following this idea, heatmap plus IoU cost design are implemented to upgrade the previous strategy. In Gaussian Area-based Heatmap and IoU Cost Positive Sample (DAHIPS) Assignment, the performance at IoU of 0.5 maintains almost the same as the previous strategy, while the most notable change is on AP at IoU of 0.8. The performance beaks through to 92.0%, which is a great improvement of 13.6% compared to 78.4% of stateof-the-art ST-MVNDet.

The above single positive label assignment strategies are based on propelling the regression loss to approach the classification loss. These type of ideas shows great validity. In this strategy, the strong binding strategy has been experimented with. Gaussian Area-based Consistent Heatmap and IoU

Cost Positive Sample (GACHIPS) Assignment inherits the previous strategy, using heatmap and IoU as cost, calculating classification loss and regression loss after finding the best-matched anchor point. The final result shows further improvement at AP of IoU 0.5 and 0.8, which increased to 97.4% and 93.9%, respectively.

The multi-positive sample strategy designed in image object detection is actually to solve problems such as missed detection. The introduction of more positive sample points makes the model better distinguish the target and the background. However, the bounding boxes belonging to different targets do not overlap in the BEV perspective detection problem. Therefore, there is no problem that some targets have fewer pixels and are difficult to identify as foreground due to overlapping targets. Introducing multiple positive samples into BEV object detection does not consider the problems it brings to the regression, that is, the reduction of regression accuracy of the model. The experimental results show that the prediction regression results of many key points identified as positive samples have a small overlap with the ground-truth box. They are located far from the center point of the ground-truth box and have prediction boxes of the same size as the groundtruth box, but there is a larger offset. The performance of this point in statistics indicates that the low-precision AP results are not much different, while the high-precision AP@IOU=0.8 result is 18.2% lower than GACHIPS. This indicates that these positive sample points have a large deviation in the loss of $l_{\triangle xy}^{reg}$ and cannot continue to optimize. This is because the offset supervision values of multiple positive samples at different key point positions are variant. The farther away from the center point, the larger the offset supervision value is. These positive sample points of the same target provide the overall loss with different gradient values. However, the gradient descent algorithm can only regress each channel of each positive sample point to the same numerical level. Positive sample points with larger offset positions need higher weights to make their predicted values closer to the ground truth value. However, to solve such problems introduced by the multi-positive sample design, the benefits are not as good as directly using the single-positive sample point design because focal loss can solve the problem of foreground and background classification in the current scene.

In the single positive sample design, a classification-guided regression strategy and classification-regression binding strategy are adopted to synchronize the contribution of classification and regression to the model's gradient. Experiments show that the original DIPS strategy defines a set of optimal positive sample points for classification and regression through artificial methods. The classification and regression of positive samples are at the center of the supervision frame. This set of artificial positive points circumvents the sample assignment operation but suffers from limited performance. Based on classification-guided regression, the GAHPS and GAHIPS experiments show better performance. Based on the training classification results of the current round, the two strategies define the position of the regression positive sample points. As the training progresses, the regression of positive sample points of the model will gradually approach the positive

sample points of classification. Unlike DIPS, because the model will regress key points other than the center point during the training process, the model has an ideal situation where the classification does not completely converge to the target center point. In other words, the classification score of the center point is not necessarily the highest. Therefore, after certain epochs of training, the model will infer the current best prediction bounding box based on the current results in the testing stage, which has the highest classification score and the smallest regression bias. In addition, it is found from the GAHIPS experimental results that when the regression prediction results are involved in sample assignment, the highprecision performance of the model is further improved. This indicates that the rotation IOU participates in model training guidance through sample assignment, further improving the model's performance. Based on this, we believe that the center point assumption should be discarded, and the allocation search of positive and negative samples in training should be carried out in a completely free manner. GACHIPS takes the sum of the heatmap and IOU decoded by each candidate point in the Gaussian region as the cost and finds the best candidate point as the positive sample point of the current target to guide the model training and maximize the consistency of classification and regression. Experiments show that this method further improves the model's overall performance and achieves a 1.9% improvement in high-precision performance.

2) Ablation Study on Interactive Transformer-based BEV Fusion Approaches: To illustrate the effectiveness of interactive transformer-based BEV fusion approaches, the fusion module is inserted into the basic network framework with DIPSA label assignment. Table II presents the results of transformers as well. In the Direct Interactive Transformer for BEV Fusion, the performance rapidly reached the same level as GAPHIPS with only slightly lower performance, around 1.6% in high precision IoU of 0.8. The Dense Query Map-based Interactive Transformer for BEV Fusion (DQMITBF) exhibits stronger performance. All three indicators exceed GAPHIPS in an all-around way. This brings the AP result of IoU 0.5, 0.65, and 0.8 to 98.8%, 97.7%, and 94.8%, respectively. Despite the huge performance improvement, we've found that the Direct Interactive Transformer module increases the inference time by about 60ms compared to GACHIPS, whose performance is the same. The DQMITBF module's parameters increase by about 4k and require 0.36 more GFLOPs.

The results of this experiment show that a reasonable fusion logic would significantly enhance the performance of our RaLiBEV. Simple cross-attention between feature maps can increase performance. Still, Query based ideas can result in better effects depending on the flexibility of weights brought in by the learnable query.

3) Performance Comparison with State-of-the-art Methods on Different Weather Conditions: Following MVDNet [17], model performance in different weather is tested in this paper as described in Table III. The simulated foggy LiDAR data is generated by the code provided by MVDNet. This experiment is set as training using clear-only and clear plus foggy LiDAR and radar data, then testing under both clear

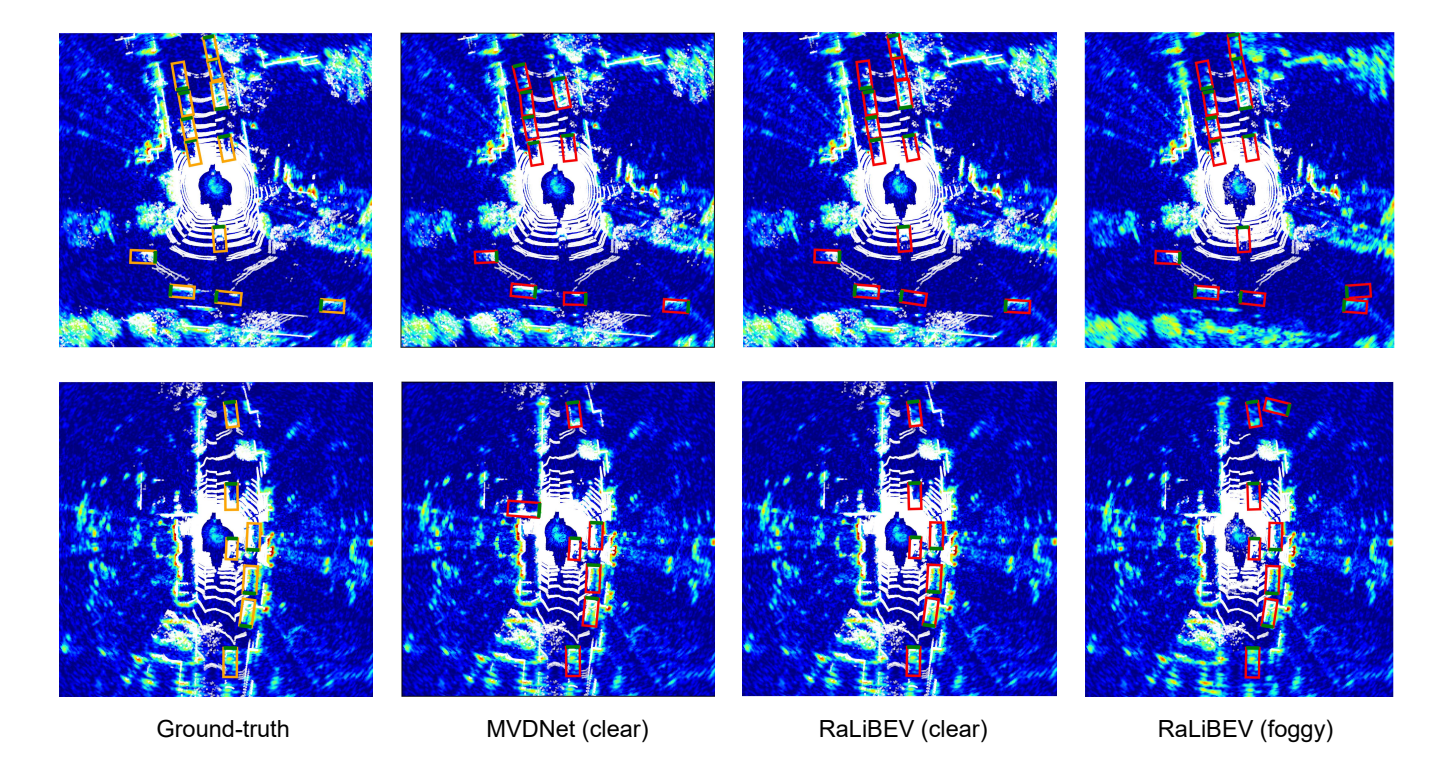


Fig. 5. Visualization of detection results of MVDNet and RaLiBEV.

and foggy data. Two peak performance models are chosen to prove their capability under this condition. One is RaLiBEV with GAPHIPS, the other is RaLiBEV with DQMITBF. The performance of GAPHIPS training under clear-only data and testing under the foggy scenario is better than DQMITBF's. The performance of the horizontal comparison model after data enhancement is about 10%. GAPHIPS increases from 84.6%, 82.4%, and 73.8% to 97.8%, 96.7%, and 93.7% under the foggy test. This result exceeds the ST-MVDNet over 20% at clear plus foggy training and foggy test scenario.

Fig. 5 shows the ground truth, MVDNet, RaLiBEV(clear), and RaLiBEV(foggy) result of 3332^{th} and 4103^{th} frame in the test dataset. The MVDNet is tested under a clear scenario. The label boxes are decorated with yellow color, and the predicted boxes by each model are decorated with red color. All boxes use green lines to illustrate the heading of the object. Each picture overlaps LiDAR with white color points and radar with pseudo-color JET and bounding boxes. It is easy to find out that the estimations of MVDNet have 3 miss detection and 4 predicted boxes with reversed heading angles in the top row figure, and 1 false alarm and 2 reversed predicted boxes in the bottom row figure. The RaLiBEV(clear) shows no error. However, the foggy result gives 1 false alarm in two subfigures, but still, no false heading angle is given.

V. CONCLUSION

In this paper, we have introduced RaLiBEV to enable vehicle detection under adverse foggy weather conditions. To enhance the performance of the model, especially for high-precision detection, novel label assignment and transformer-based fusion strategies are proposed. Specifically, the Gaussian

Area-based Consistent Heatmap and IOU Cost Positive Sample Assignment (GACHIPS) strategy is proposed to dynamically adjust the classification and regression positive sample position, to solve the inconsistency problem in the loss procedure. Meanwhile, the Dense Query Map-based Interactive Transformer for BEV Fusion (DQMITBF) is proposed to aggregate more aligned features from different sensor data. Due to the introduction of the dense learnable query in the fusion module, RaLiBEV can fuse the features from radar and LiDAR in a more flexible way. The experiments with ORR dataset show that RaLiBEV exceeds all existing state-of-theart approaches by a large margin.

REFERENCES

- [1] D. Barnes, M. Gadd, P. Murcutt, P. Newman, and I. Posner, "The oxford radar robotcar dataset: A radar extension to the oxford robotcar dataset," in *Proceedings of IEEE International Conference on Robotics and Automation (ICRA)*, 2020, pp. 6433-6438.
- [2] A. Li, S. Chen, L. Sun, N. Zheng, M. Tomizuka and W. Zhan, "SceGene: Bio-inspired traffic scenario generation for autonomous driving testing," *IEEE Transactions on Intelligent Transportation Systems*, vol. 23, no. 9, pp. 14859-14874, Sep. 2022.
- [3] Y. Tang, C. Zhao, J. Wang, C. Zhang, Q. Sun, W. X. Zheng, W. Du, F. Qiao, and J. Kurths, "Perception and navigation in autonomous systems in the era of learning: a survey," *IEEE Transactions on Neural Networks and Learning Systems*, April 2022, doi: 10.1109/TNNLS.2022.3167688.
- [4] Z. Wang, J. Zhan, C. Duan, X. Guan, P. Lu, and K. Yang, "A review of vehicle detection techniques for intelligent vehicles," *IEEE Transactions on Neural Networks and Learning Systems*, Jan. 2022, doi: 10.1109/TNNLS.2021.3128968.
- [5] D. J. Fremont, E. Kim, Y. V. Pant, S. A. Seshia, A. Acharya, X. Bruso, P. Wells, S. Lemke, Q. Lu, and S. Mehta. "Formal

- scenario-based testing of autonomous vehicles: From simulation to the real world," in *Proceedings of the IEEE 23rd International Conference on Intelligent Transportation Systems (ITSC)*, 2020, pp. 1-8.
- [6] S. Chen, B. Liu, C. Feng, C. Vallespi-Gonzalez, and C. Wellington, "3d point cloud processing and learning for autonomous driving: Impacting map creation, localization, and perception," *IEEE Signal Processing Magazine*, vol. 38, no. 1, pp. 68-86, Jan. 2021.
- [7] Y. Li, L. Ma, Z. Zhong, F. Liu, M. A. Chapman, D. Cao, and J. Li, "Deep learning for lidar point clouds in autonomous driving: A review," *IEEE Transactions on Neural Networks and Learning Systems*, vol. 32, no. 8, pp. 3412-3432, Aug. 2020.
- [8] A. H. Lang, S. Vora, H. Caesar, L. Zhou, J. Yang, and O. Beijbom, "Pointpillars: Fast encoders for object detection from point clouds," in *Proceedings of the IEEE/CVF Conference on Computer Vision and Pattern Recognition (CVPR)*, 2019, pp. 12697-12705.
- [9] T. Yin, X. Zhou, and P. Krahenbuhl, "Center-based 3D object detection and tracking," in *Proceedings of the IEEE/CVF Con*ference on Computer Vision and Pattern Recognition (CVPR), 2021, pp. 11784-11793.
- [10] J. Liu, L. Bai, Y. Xia, T. Huang, B. Zhu, and Q. -L. Han, "GNN-PMB: A simple but effective online 3D multi-object tracker without bells and whistles," *IEEE Transactions on Intelligent Vehicles*, Oct. 2022, doi: 10.1109/TIV.2022.3217490.
- [11] P. Dahal, S. Mentasti, S. Arrigoni, F. Braghin, M. Matteucci, and F. Cheli, "Extended object tracking in curvilinear road coordinates for autonomous driving," *IEEE Transactions on In*telligent Vehicles, May 2022, doi: 10.1109/TIV.2022.3171593.
- [12] S. Liang, Z. Cao, C. Wang, and J. Yu, "Hierarchical estimation-based lidar odometry with scan-to-map matching and fixed-lag smoothing," *IEEE Transactions on Intelligent Vehicles*, May 2022, doi: 10.1109/TIV.2022.3173665.
- [13] H. Guo, J. Zhu, and Y. Chen, "E-LOAM: LiDAR odometry and mapping with expanded local structural information," *IEEE Transactions on Intelligent Vehicles*, Feb. 2022, doi: 10.1109/TIV.2022.3151665.
- [14] C. Lin, D. Tian, X. Duan, J. Zhou, D. Zhao, and D. Cao, "3D-DFM: Anchor-free multimodal 3-D object detection with dynamic fusion module for autonomous driving," *IEEE Trans*actions on Neural Networks and Learning Systems, May 2022, doi: 10.1109/TNNLS.2022.3171553.
- [15] Y. Chen, H. Li, R. Gao, and D. Zhao, "Boost 3-D object detection via point clouds segmentation and fused 3-D GIoU-L1 loss," *IEEE Transactions on Neural Networks and Learning Systems*, vol. 33, no. 2, pp. 762-773, Feb. 2022.
- [16] S. C. Huang, Q. V. Hoang, and T. H. Le, "SFA-Net: A selective features absorption network for object detection in rainy weather conditions," *IEEE Transactions on Neural Networks and Learning Systems*, Jan. 2022, doi: 10.1109/TNNLS.2021.3125679.
- [17] K. Qian, S. Zhu, X. Zhang, and L. E. Li, "Robust multimodal vehicle detection in foggy weather using complementary lidar and radar signals," in *Proceedings of the IEEE/CVF Conference* on Computer Vision and Pattern Recognition (CVPR), 2021, pp. 444-453.
- [18] Y. J. Li, J. Park, M. O'Toole, and K. Kitani, "Modality-agnostic learning for radar-lidar fusion in vehicle detection," in Proceedings of the IEEE/CVF Conference on Computer Vision and Pattern Recognition (CVPR), 2022, pp. 918-927.
- [19] S. Li, C. H. He, H. Chen, R. H. Li, and L. Zhang, "A dual weighting label assignment Scheme for Object Detection," in Proceedings of the IEEE/CVF Conference on Computer Vision and Pattern Recognition (CVPR), 2022, pp. 9387-9396.
- [20] C. R. Qi, H. Su, K. Mo, and L. J. Guibas, "Pointnet: Deep learning on point sets for 3d classification and segmentation," in *Proceedings of IEEE Conference Computer Vision Pattern Recognition (CVPR)*, 2017, pp. 652–660.

- [21] C. R. Qi, L. Yi, H. Su, and L. J. Guibas, "Pointnet++: Deep hierarchical feature learning on point sets in a metric space," in *Proceedings of the Conference on Advances in Neural Infor*mation Processing Systems (NeurIPS), 2017, pp. 5099–5108.
- [22] D. Maturana and S. Scherer, "Voxnet: A 3d convolutional neural network for real-time object recognition," in *Proceedings of IEEE/RSJ International Conference on Intelligent Robots and Systems (IROS)*, 2015, pp. 922-928.
- [23] W. Shi and R. Rajkumar, "Point-GNN: Graph neural network for 3d object detection in a point cloud," in *Proceedings of the IEEE/CVF Conference on Computer Vision and Pattern Recognition (CVPR)*, 2020, pp. 1711-1719.
- [24] J. S. Hu, T. Kuai, and S. L. Waslander, "Point density-aware voxels for lidar 3d object detection," in *Proceedings of the IEEE/CVF Conference on Computer Vision and Pattern Recognition (CVPR)*, 2022, pp. 8469-8478.
- [25] M. Kronauge and H. Rohling, "Fast two-dimensional CFAR procedure," *IEEE Transactions on Aerospace and Electronic Systems*, vol. 49, no. 3, pp. 1817-1823, July 2013.
- [26] S. Lim, S. Lee, and S. -C. Kim, "Clustering of detected targets using DBSCAN in automotive radar systems," in *Proceedings* of the 19th International Radar Symposium (IRS), 2018, pp. 1-7.
- [27] A. Danzer, T. Griebel, M. Bach, and K. Dietmayer, "2D car detection in radar data with PointNets," in *Proceedings of the IEEE International Conference on Intelligent Transportation Systems (ITSC)*, 2019, pp. 61–66.
- [28] J. Liu, W. Xiong, L. Bai, Y. Xia, T. Huang, W. Ouyang, and B. Zhu, "Deep instance segmentation with automotive radar detection points," *IEEE Transactions on Intelligent Vehicles*, April 2022, doi: 10.1109/TIV.2022.3168899.
- [29] W. Xiong, J. Liu, Y. Xia, T. Huang, B. Zhu, and W. Xiang, "Contrastive learning for automotive mmWave radar detection points based instance segmentation," in *Proceedings of the IEEE International Conference on Intelligent Transportation Systems (ITSC)*, 2022, pp. 1255-1261.
- [30] K. Patel, K. Rambach, T. Visentin, D. Rusev, M. Pfeiffer, and B. Yang, "Deep learning-based object classification on automotive radar spectra", in *Proceedings of the IEEE Radar Conference (RadarConf)*, 2019, pp. 1-6.
- [31] A. Cozma, L. Morgan, M. Stolz, D. Stoeckel, K. Rambach, "DeepHybrid: Deep learning on automotive radar spectra and reflections for object classification," in *Proceedings of IEEE Intelligent Transportation Systems Conference (ITSC)*, 2021, pp. 2682-2687.
- [32] M. Bijelic, T. Gruber, F. Mannan, F. Kraus, W. Ritter, K. Dietmayer, and F. Heide, "Seeing through fog without seeing fog: Deep multimodal sensor fusion in unseen adverse weather," in *Proceedings of the IEEE/CVF Conference on Computer Vision and Pattern Recognition (CVPR)*, 2020, pp. 11682-11692.
- [33] A. Bochkovskiy, C. Wang, and H. M. Liao, "YOLOv4: Optimal speed and accuracy of object detection," 2020, ArXiv:2004.10934.
- [34] T.-Y. Lin, P. Goyal, R. Girshick, K. He, and P. Dollár, "Focal loss for dense object detection," in *Proceedings of the IEEE International Conference on Computer Vision (ICCV)*, 2017, pp. 2980-2988.
- [35] D. Erhan, C. Szegedy, A. Toshev, and D. Anguelov "Scalable object detection using deep neural networks," in *Proceedings* of the IEEE Conference on Computer Vision and Pattern Recognition (CVPR), 2014, pp. 2147-2154.
- [36] N. Carion, F. Massa, G. Synnaeve, N. Usunier, A. Kirillov, and S. Zagoruyko, "End-to-end object detection with transformers," in *Proceedings of the European Conference on Computer Vision* (ECCV), 2020, pp. 213-229.
- [37] A. Vaswani, N. Shazeer, N. Parmar, J. Uszkoreit, L. Jones, A. N. Gomez, Ł. Kaiser, and I. Polosukhin, "Attention is all you need," in *Proceedings of the Conference on Advances in*

- Neural Information Processing Systems (NeurIPS), 2017, pp. 5998–6008.
- [38] A. Laddha, S. Gautam, S. Palombo, S. Pandey, and C. Vallespi-Gonzalez, "Mvfusenet: Improving end-to-end object detection and motion forecasting through multi-view fusion of lidar data," in *Proceedings of the IEEE/CVF Conference on Computer Vision and Pattern Recognition (CVPR)*, 2021, pp. 2865-2874.